Assessment of pressure-assisted sintering models through sinter-forging tests: A case study of alumina incorporating capillarity forces

Charles Manière, Christelle Harnois, Christophe Couder, Christelle Bilot, Sylvain Marinel

Assessment of pressure-assisted sintering models through sinter-forging tests: a case study of alumina incorporating capillarity forces

Charles Manière[1]*, Christelle Harnois[1], Christophe Couder[1], Christelle Bilot[1], Sylvain Marinel[1]

1. Normandie Univ, ENSICAEN, UNICAEN, CNRS, CRISMAT, 14000, Caen, France

Keywords
Pressure assisted sintering; Ceramic; Modeling; Creep; Mechanisms

Abstract

Pressure-assisted sintering models involve numerous closely correlated parameters that depend on temperatures, porosity, and microstructure development. Consequently, the identification of the model parameters is relatively lengthy and requires experiments to extract the underlying creep behavior (pressure/temperature dependent), shear, bulk sintering moduli that are porosity-dependent, and grain growth. Knowing that certain sintering mechanisms are grain-size dependent, it is very difficult to assess the densification behavior for the case of ceramics. We have already developed a sinter-forging method to assess independently all parameters for ceramics. However, this method implies numerous interruption tests to measure the specimen diameter evolution, and the capillarity forces were neglected. In this study, an instrumented microwave sinter-forging prototype avoiding highly repetitive interruption tests has been developed to record the specimen diameter evolution of submicronic alumina powder samples. The new method includes the effect of the capillarity forces on the identification equations, making the model more realistic for submicronic ceramics. The resulting model was tested on a finite element code for validation and to explore its stability for complex shapes.

Graphical Abstract

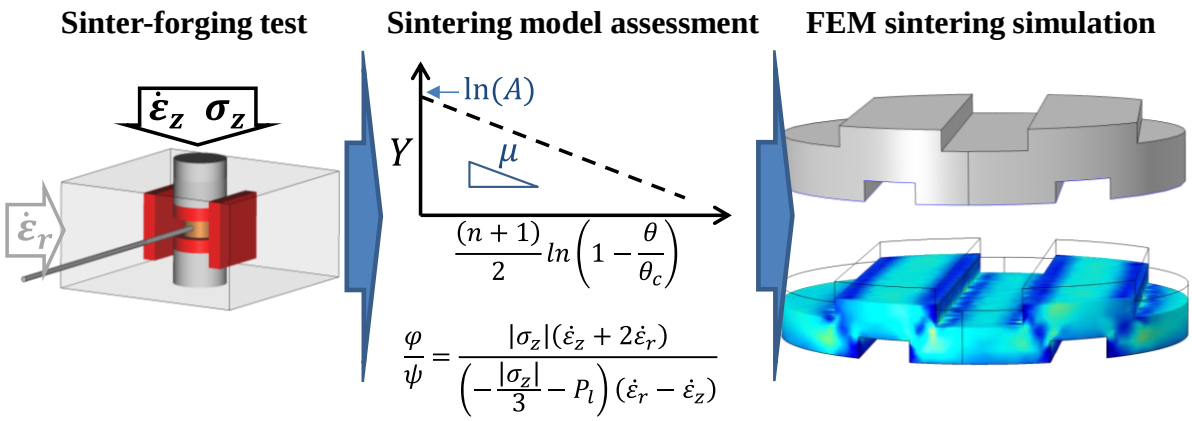

* Corresponding author: **CM**: Laboratoire de cristallographie et sciences des matériaux (CRISMAT), 6 Bvd du maréchal Juin 14050 CAEN CEDEX 4, France
Ph.: +33.2.31.45.13.69 ; *E-mail address*: charles.maniere@ensicaen.fr

Highlights

- Pressure assisted sintering model assessment
- Identification including the capillarity forces
- Instrumented porous stage method insensitive to grain growth

Nomenclature

Alphabetical terms and abbreviations

A Creep law deformability term ($Ks^{-1}Pa^{-n}$)
A_0 Deformability pre-exponential factor ($Ks^{-1}Pa^{-n}$)
D Diffusion coefficient ($m^2.S^{-1}$)
$\dot{e}$ Trace of the strain rate tensor (s^{-1})
$\mathbb{i}$ Identity tensor
n Creep law stress exponent
P_I Sintering stress ($N.m^{-2}$)
r Particles radius (m)
T Temperature (K)
HIP Hot isostatic pressing
SPS Spark Plasma Sintering
HP Hot pressing
SF Sinter-forging
a, b, c Fitting constants
t Time (s)
$\underline{s}$ Deviatoric stress tensor ($N.m^{-2}$)
P Hydrostatic stress ($N.m^{-2}$)

Greek symbols
θ Porosity
$\dot{\theta}$ Porosity elimination rate (s^{-1})
ρ Relative density
$\underline{\sigma}$ Stress tensor ($N.m^{-2}$)
σ_{eq} Equivalent stress ($N.m^{-2}$)
$\underline{\dot{\varepsilon}}$ Strain rate tensor (s^{-1})
$\dot{\varepsilon}_{eq}$ Equivalent strain rate (s^{-1})

φ Shear modulus

ψ Bulk modulus

α Surface energy (J.m^{-2})

$\dot{\gamma}$ Shear strain rate invariant (s^{-1})

$\dot{\varepsilon}_z$ Axial strain rate tensor component (s^{-1})

$\dot{\varepsilon}_r$ Radial strain rate tensor component (s^{-1})

σ_r Radial stress tensor component (N.m^{-2})

σ_z Axial stress tensor component (N.m^{-2})

θ_c Critical porosity

μ Bulk modulus exponent

$\#_{1\ or\ 2}$ the subscripts 1 or 2 refer to parameters at different pressures

1. Introduction

Pressure-assisted sintering methods, such as Hot Isostatic Pressing (HIP) or Spark Plasma Sintering (SPS), play a pivotal role in sintering high-performance materials. The application of pressure facilitates a reduction in the sintering temperature, thereby preserving submicronic grain sizes. Additionally, it facilitates the complete elimination of porosity, enabling the fabrication of transparent ceramics, and aids in sintering ultra-refractories with minimal or no sintering additives [1,2,11,3–10]. However, pressure-assisted sintering encompasses diverse mechanisms highly sensitive to applied stress, grain size, and temperature [6,12]. Deformation/sintering maps [13–15], for instance, assist in identifying temperature and pressure zones where various sintering mechanisms prevail over others. Mechanisms such as grain boundary/lattice diffusion/grain boundary sliding exhibit varying sensitivity to grain size, while others like dislocation creep are generally assumed to be grain size independent [6].

In ceramics, the final stage grain growth is a critical factor, significantly disturbing the underlying creep mechanisms. For instance, a grain size increase of twice involves a grain-boundary diffusion mechanism rate divided by a factor of 8. In many ceramics, final stage grain growth surpasses twice the initial grain size which substantially disrupts sintering mechanisms [16]. Consequently, identifying the underlying creep mechanism during pressure-assisted

sintering of ceramics cannot rely on the creep data of bulk materials like it is done for metals [17–25] that often exhibit grain size-independent mechanisms (dislocation-based).

The high sensitivity of ceramics sintering behaviors to grain growth is one of the greatest obstacles of ceramic models assessment that prevents the direct identification by mechanical tests. To partially solve this problem, we have developed methods capable of assessing both the creep and densification parameters directly from porous stage tests (far from grain growth zone). A first method[26,27] is based on the kinetic fields [28] (or master sintering curves[29,30]). It involves initially the identification of the sintering activation energy from various heating rate tests, followed by a parametric regression [31] study to calibrate the moduli using the independently identified activation energy as a reference. While this method is relatively fast and efficient, we have developed an isobar/isotherm method based on sinter-forging tests [16] to ensure identifying sintering behavior reflecting the reality of the porous skeleton. This unique method allows the assessment of sintering parameters without the risk of grain growth disturbance and provides valuable experimental shear and bulk moduli data for zirconia, facilitating the reproduction of highly responsive sintering densification curves observed in flash spark plasma sintering [32]. Furthermore, coupling these experimental moduli with mesoscale simulation aids in studying surface diffusion effects [33–36] by comparing different possible porosity geometries [32]. However, this method [16] necessitates knowledge of the diameter expansion of the sinter-forged sample, involving numerous repetitive interrupted tests to record the sample diameter evolution and it neglects the capillarity forces. The grain growth independent sintering identification method is still very long and highly sensitive to experimental errors by the number of tests required to assess the specimen diameter.

In this study, we present an experimental and fully instrumented sinter-forging prototype designed to record *in situ* the specimen diameter evolution. This prototype was mounted on a press-equipped microwave oven, enabling the imposition of high heating rates comparable to those commonly applied in the spark plasma sintering process. In addition, the set of identification equations has been adapted to take into account the capillary forces present in

most submicronic ceramic powders. This new assessment method provides a valuable solution to identify the sintering simulation parameters from mechanical tests without grain growth disturbance, reductive hypotheses and with a reliable experimental protocol.

This article is organized as follows: the experimental prototype and starting powder are presented first. Afterward, the model main equations and their rearranging to obtain the sinter-forging assessment equations is presented with, in the next section, the complete description of the 4-step identification method proposed. The experimental curves, identification and modeling verification are presented in the results section. In the end, a complex shapes simulation case is tested (using the identified parameters) to illustrate the simulation possibilities.

2. Experiment and method

2.1. Instrumented sinter-forging prototype

The original identification equations use sinter-forging tests to identify all the sintering parameters from porous specimens. Specifically, these equations require the separate identification of shear and bulk behaviors, necessitating a system of two equations. While different sintering test couples, such as hot pressing (HP)/sinter-forging (SF) or hot isostatic pressing (HIP)/sinter-forging (SF), can be employed to separate these behaviors, this approach increases the number of tests and introduces errors between them. To address this, alternative methods utilize instrumented single tests with stress/displacement data in axial and radial directions, allowing the establishment of a system of two equations capable of simultaneously identifying shear and bulk behaviors. For instance, a hot pressing test with information on the radially developed stress is employed to identify the porous plasticity model of cold compaction. A similar approach is used by Geindreau *et al* [20], to identify lead sintering. We have also employed a similar strategy for virtually identifying the moduli from mesoscale

simulations [32]. However, for ceramics, the high temperature sensitivity of pressure sensors makes this experimental approach challenging.

In this context, sinter-forging serves as a viable alternative, applicable in classic hot pressing devices without dies, where specimen diametric expansion can be easily obtained using a contour camera or, as in this study, a contact displacement sensor. The microwave energy in this work is employed to control the heating of the pressing device. This microwave sinter-forging prototype is particularly interesting as it allows control over slow to fast heating rates, ranging from conventional 5K/min to spark plasma sintering 100K/min. Through the use of silicon carbide susceptors, heating can be homogeneously imposed to the specimens.

The microwave press device is supplied by SAIREM® (SAIREM® LABOTRON IWASP2000 2TE). A 2.45 GHz solid-state microwave generator (SAIREM® GMS1000MS) is utilized with an auto-adaptive PID regulator (SAIREM® EUROTHERM2408). As alumina poorly interacts with microwaves, SiC susceptors are positioned on the upper and lower punches in contact with the specimen. These susceptors heat and compensate for the cooling fluxes resulting from the punches. To minimize lateral cooling, two SiC susceptors are added on the sides of the specimen (see configuration in figure 1a). The device records the specimen surface temperature with a pyrometer pointing at the sample. On the other side, an alumina plunger is added to record the radial displacement using a displacement sensor magnescale DS830SLR[37] (figure 1a). The sinter-forging test employs isobar/isotherm tests, and the axial/radial displacement curves are calculated from the final specimen dimensions.

To maximize sintering amplitude, a heating rate of 100K/min is selected, and pressure is applied at the beginning of the temperature dwell (see cycle in figure 1b).

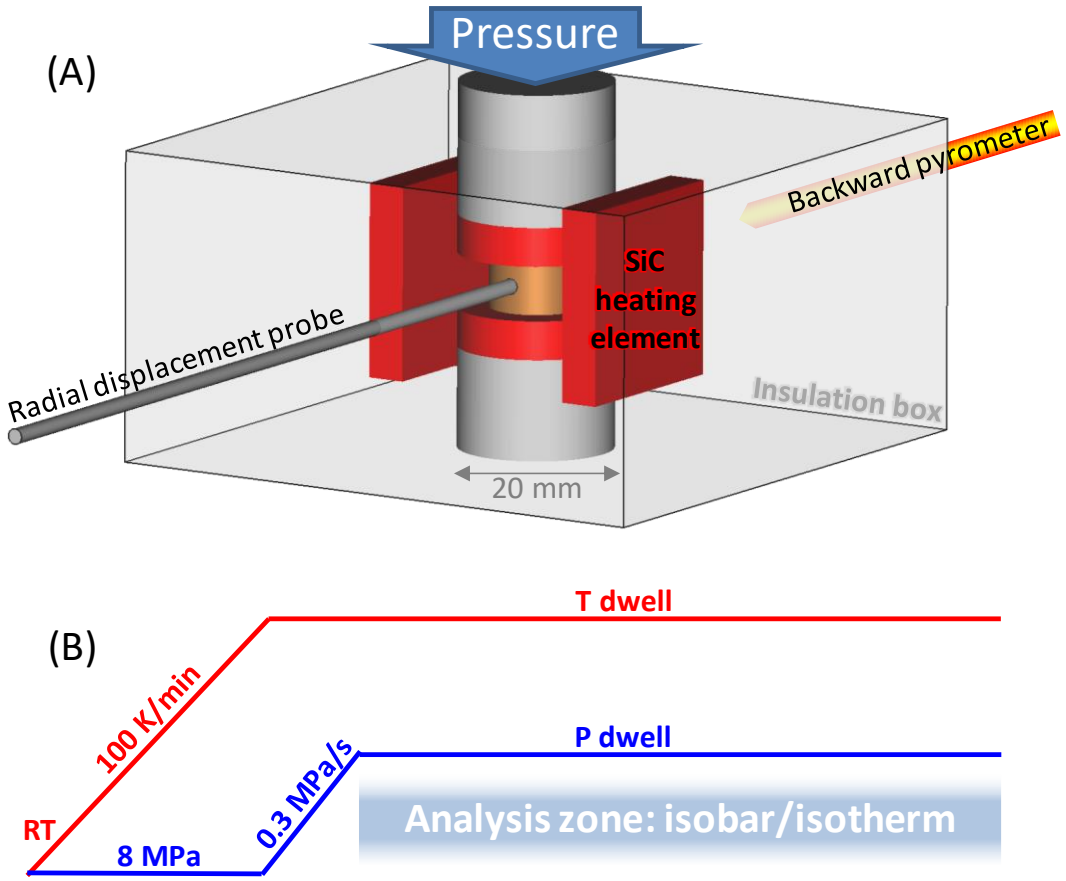

Figure 1 (A) Scheme of the microwave sinter-forging prototype designed to heat a ceramic specimen by SiC susceptors from the sides, upper and lower punches while allows the diameter expansion measurement and a backward temperature measurement by pyrometer; the sinter-forging curves should be in isotherm and isobar conditions, the cycle presented in (B) apply the pressure at the beginning of the dwell to preserve a maximum of sintering amplitude and a 100K/min cycle is used to study similar conditions of advanced methods like the spark plasma sintering.

2.2. Materials

A submicronic alumina powder (Baikowski® BMA15) is used for the sinter-forging of presintered Ø12, h8 mm samples. This alumina grade is 100% α crystalline phase, with a specific surface of 15 m^2/g, a d50 of 0.12 µm and a high purity of 99.99%. With the BMA15 alumina powder, the explored temperature range (where sintering is active) is 1000, 1100, and 1200°C at 30MPa. For the 1200°C temperature, another test is conducted to identify the stress exponent [38]. The details of the sintering model governing equation and the assessment method is provided in the next section.

3. Theory and calculations

3.1. Sintering model and sinter-forging test equations

The sintering of 3D objects or of complex hot pressing devices can be simulated by the finite element method (FEM). The commercial software COMSOL multiphysics® is used to draw/import the geometry, discretize it by an automatic meshing module, affect motions and pressure boundary conditions, compute and treat the simulation results. The main equation of the continuum theory of sintering[39,40] implemented in the software is the following:

$$\underline{\dot{\varepsilon}} = A(T)\sigma_{eq}{}^{n-1}\left(\frac{\underline{S}}{\varphi} + \frac{(P-P_l)}{3\psi}\,\underline{\underline{\mathbb{1}}}\right) \quad (1)$$

With *A* the temperature dependent creep term which has the following expression in the grain growth inactive zone.

$$A(T) = A_0\frac{\exp(\frac{-Q}{RT})}{T} \quad (2)$$

P_l is the sintering stress that can be modeled by Skorohod's theoretical[40] expression which depends on the porosity, surface energy (1.12 J/m^2 for alumina [41]) and the particle radius that can be assumed constant in high porosity tests where grain growth is limited.

$$P_l = \frac{3\alpha}{r}(1-\theta)^2 \quad (3)$$

For the case of sinter-forging and assuming no friction, a homogenous temperature, the specimen has a stress only in axial direction and the same displacement in radial direction.

$$\underline{\sigma} \equiv \begin{pmatrix} 0 & 0 & 0 \\ 0 & 0 & 0 \\ 0 & 0 & \sigma_z \end{pmatrix}; \underline{\dot{\varepsilon}} \equiv \begin{pmatrix} \dot{\varepsilon}_r & 0 & 0 \\ 0 & \dot{\varepsilon}_r & 0 \\ 0 & 0 & \dot{\varepsilon}_z \end{pmatrix} \quad (4)$$

The analytical formulation of sinter-forging can be calculated from equations (1) and (4). Taking into account the sintering stress P_l, the analytic model is describing the axial and radial strain rates, which are detailed in ref [16] and have the following form.

$$\dot{\varepsilon}_z = A\left(\frac{\frac{2|\sigma_z|^2}{3\varphi} + \frac{\left(-\frac{|\sigma_z|}{3} - P_l\right)^2}{\psi}}{1-\theta}\right)^{\frac{n-1}{2}}\left(-\frac{2|\sigma_z|}{3\varphi} + \frac{\left(-\frac{|\sigma_z|}{3} - P_l\right)}{3\psi}\right) \quad (5)$$

$$\dot{\varepsilon}_r = A\left(\frac{\frac{2|\sigma_z|^2}{3\varphi}+\frac{\left(-\frac{|\sigma_z|}{3}-P_l\right)^2}{\psi}}{1-\theta}\right)^{\frac{n-1}{2}}\left(\frac{|\sigma_z|}{3\varphi}+\frac{\left(-\frac{|\sigma_z|}{3}-P_l\right)}{3\psi}\right) \quad (6)$$

3.2. Stress exponent "n" identification

There are numerous ways to identify the stress exponent like creep tests on dense specimens[18,19], and sintering tests at different pressures and close porosities [31,42]. In a previous study [38], we compared the "stepwise" method applied to Spark Plasma Sintering (SPS), also known as multi-step pressure dilatometry [42], with a sinter-forging test method at constant porosity. We demonstrated that all methods converge to similar values for alumina, and the method should incorporate the sintering stress if the powder is submicronic (P_l is not negligible). The latter method is preferred in the present work, which focuses on sinter-forging. The identification equation for the stress exponent is determined as follows.

The method involves conducting two sinter-forging tests at the same temperature but with different pressures. At a fixed relative density, the axial strain rates are measured for the two pressures ($\dot{\varepsilon}_1$, $\dot{\varepsilon}_2$). The value of "n" is then determined by the ratio of these strain rates using the following identification equation[38].

$$n = 1 + \frac{ln\left(\frac{\dot{\varepsilon}_1}{\dot{\varepsilon}_2}\left(\frac{-\frac{2|\sigma_2|}{3\varphi}+\frac{\left(-\frac{|\sigma_2|}{3}-P_l\right)}{3\psi}}{-\frac{2|\sigma_1|}{3\varphi}+\frac{\left(-\frac{|\sigma_1|}{3}-P_l\right)}{3\psi}}\right)\right)}{ln\sqrt{\frac{\frac{2|\sigma_1|^2}{3\varphi}+\frac{\left(-\frac{|\sigma_1|}{3}-P_l\right)^2}{\psi}}{\frac{2|\sigma_2|^2}{3\varphi}+\frac{\left(-\frac{|\sigma_2|}{3}-P_l\right)^2}{\psi}}}} \quad (7)$$

For the BMA15 alumina powder, considering the sintering stress P_l, a stress exponent value (n) of 2.3 has been previously identified [38]. This value is retained for this study, which utilizes the same powder. In the following sections, detailed identification equations for determining all other sintering parameters (φ, ψ, A) from sinter-forging tests are provided. Similar to a previous approach [16], the method relies on sinter-forging, using the axial and radial displacements that can be experimentally measured. In this new approach, the equation

incorporates the sintering stress P_l. This updated approach allows exploration of lower applied pressures where the sintering stress competes with the applied stress. Moreover, this method is highly recommended for nano/submicronic powders with significant capillarity stresses, a common scenario in ceramics

3.3. Identification of the moduli φ, ψ and A

The method uses the axial and radial displacement data so equations (5) and (6) are the main starting point of this approach. Taking (5)/(6) and rearranging them, we obtain:

$$\dot{\varepsilon}_z\left(\frac{|\sigma_z|}{3\varphi}+\frac{\left(-\frac{|\sigma_z|}{3}-P_l\right)}{3\psi}\right)=\dot{\varepsilon}_r\left(-\frac{2|\sigma_z|}{3\varphi}+\frac{\left(-\frac{|\sigma_z|}{3}-P_l\right)}{3\psi}\right) \quad (8).$$

Isolating the ratio φ/ψ, we have:

$$\frac{\varphi}{\psi}=\frac{|\sigma_z|(\dot{\varepsilon}_z+2\dot{\varepsilon}_r)}{\left(-\frac{|\sigma_z|}{3}-P_l\right)(\dot{\varepsilon}_r-\dot{\varepsilon}_z)} \quad (9).$$

Inserting (9) in (5) and rearranging them, we have:

$$\varphi=\left(\frac{A(T)}{\dot{\varepsilon}_z}\right)^{\frac{2}{n+1}}\left(\frac{\frac{2|\sigma_z|^2}{3}+\frac{|\sigma_z|(\dot{\varepsilon}_z+2\dot{\varepsilon}_r)\left(-\frac{|\sigma_z|}{3}-P_l\right)}{(\dot{\varepsilon}_r-\dot{\varepsilon}_z)}}{1-\theta}\right)^{\frac{n-1}{n+1}}\left(-\frac{2|\sigma_z|}{3}+\frac{|\sigma_z|(\dot{\varepsilon}_z+2\dot{\varepsilon}_r)}{3(\dot{\varepsilon}_r-\dot{\varepsilon}_z)}\right)^{\frac{2}{n+1}} \quad (10).$$

The shear modulus is a porosity function that can be described by the following equation with θ_c a value slightly higher than the initial porosity [16,43] and μ an adjustable exponent to be determined experimentally.

$$\varphi=\left(1-\frac{\theta}{\theta_c}\right)^{\mu} \quad (11)$$

Inserting (11) in (10) and rearranging, we obtain the following identification equation.

$$Y=-\frac{(n+1)}{2}ln\left(\left(\frac{\frac{2|\sigma_z|^2}{3}+\frac{|\sigma_z|(\dot{\varepsilon}_z+2\dot{\varepsilon}_r)\left(-\frac{|\sigma_z|}{3}-P_l\right)}{(\dot{\varepsilon}_r-\dot{\varepsilon}_z)}}{1-\theta}\right)^{\frac{n-1}{n+1}}\left(-\frac{2|\sigma_z|}{3\dot{\varepsilon}_z}+\frac{|\sigma_z|(\dot{\varepsilon}_z+2\dot{\varepsilon}_r)}{3\dot{\varepsilon}_z(\dot{\varepsilon}_r-\dot{\varepsilon}_z)}\right)^{\frac{2}{n+1}}\right)=ln\big(A(T)\big)-$$

$$\mu\left(\frac{(n+1)}{2}ln\left(1-\frac{\theta}{\theta_c}\right)\right) \quad (12)$$

If the stress exponent "*n*" is identified separately and with the axial and radial experimental data of the sinter-forging test (giving $\dot{\varepsilon}_z$, $\dot{\varepsilon}_r$, θ), all the terms of the left-hand side called "*Y*" can be calculated. From the right-hand side, the term $\frac{(n+1)}{2} ln\left(1-\frac{\theta}{\theta_c}\right)$ can be calculated using $\theta_c = \theta_{initial} + 0.1$ [16,43].

Consequently, using an isobar/isotherm sinter-forging test and plotting the following linear regression equation (13), the shear modulus φ can be obtained by the slope giving the exponent "μ" and the origin gives $ln(A)$ for this temperature.

$$Y = f\left(\frac{(n+1)}{2} ln\left(1-\frac{\theta}{\theta_c}\right)\right) \quad (13)$$

The remaining unknown is the bulk modulus ψ. The latter can be determined from the shear modulus φ and the axial and radial strain rates of the same sinter-forging test using equation (9).

3.4. Sintering model parameters identification method in 4 steps

The methodology used in this paper to identify the sintering parameters is summarized in figure 2. The experimental identification method is divided in four main steps.

- Step 1 is the treatment of the experimental data that are the axial/radial displacements giving the specimen height and diameter evolution and the applied axial force. From these inputs data, the axial and radial strain rates can be calculated from the displacement rates. The true stress can be calculated with the information of the sample diameter curve and the porosity can be assessed with the dimensional data and the theoretical density of alumina 3.98 g.cm^{-3}. The axial/radial strain rates, the true stress and the porosity determination allows assessing all the sintering parameters.
- Step 2 consists in the identification of the model stress exponent "*n*" from two sinter-forging tests at the same temperature but with different pressures. At fixed porosity, equation (7) can be used to identify the "*n*" from the porosity elimination rates ratio of

the two tests. As explained earlier, this part of the study has been done in a previous work [38] giving n=2.3.

- In step 3, the identification of the shear modulus exponent "μ" and the A creep term is done using, respectively, the slope and origin of the linear regression equation (12). This regression is made for all the sinter-forging tests to have the temperature evolution of A. Typically, as the moduli are unique porosity functions in close conditions, the "μ" values (slope) are expected to be closed for the different temperature tests and in the curve fitting, a fix value is often selected. To identify the A_0 and Q values of the A creep term, the logarithm of equation (2) is used to plot the linear regression of $ln(A)$ *vs* $1/RT$. The slope gives Q and the origin gives $ln(A_0)$.

- The last remaining parameter is the bulk modulus ψ. Step 4 is the identification of this modulus using equation (9) where the axial/radial strain rate ratio and the previously determined shear modulus are used. In equations (7), (9) and (12), the sintering stress Pl is calculated using equation (3).

Step 1: Sinter-forging instrumented experiments

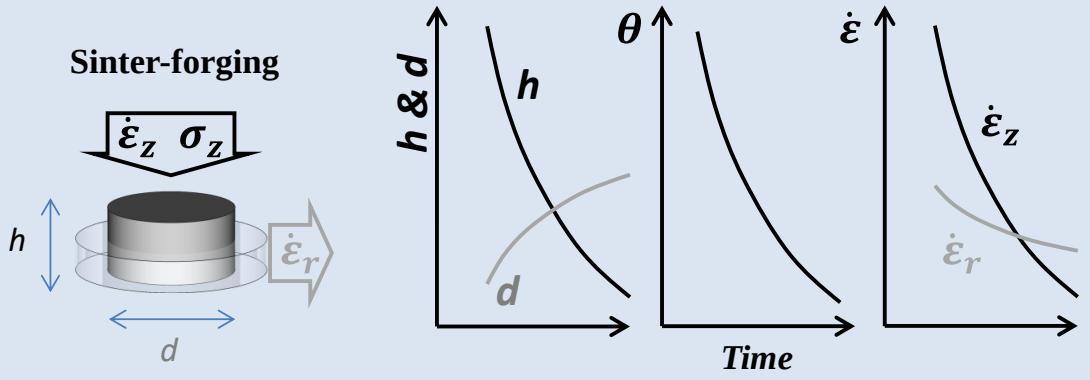

$$\dot{\varepsilon}_z = \frac{\dot{h}}{h} \qquad \dot{\varepsilon}_r = \frac{\dot{d}}{d} \qquad \sigma_z = \frac{Force(N)}{\pi(d/2)^2} \qquad \theta = 1 - (1 - \theta_{final})\left(\frac{d_{final}}{d}\right)^2 \frac{h_{final}}{h}$$

Step 2 : Identification of *n* stress exponent at constant porosity

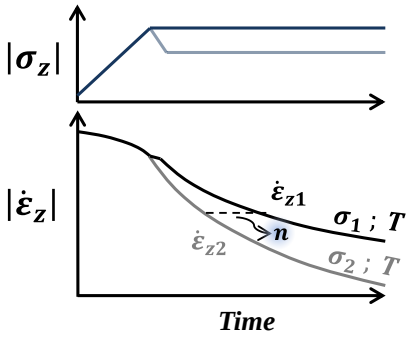

$$n = 1 + \frac{ln\left(\frac{\dot{\varepsilon}_{z1}}{\dot{\varepsilon}_{z2}}\left(\frac{-\frac{2|\sigma_2|}{3\varphi} + \frac{\left(-\frac{|\sigma_2|}{3} - P_l\right)}{3\psi}}{-\frac{2|\sigma_1|}{3\varphi} + \frac{\left(-\frac{|\sigma_1|}{3} - P_l\right)}{3\psi}}\right)\right)}{ln\sqrt{\frac{\frac{2|\sigma_1|^2}{3\varphi} + \frac{\left(-\frac{|\sigma_1|}{3} - P_l\right)^2}{\psi}}{\frac{2|\sigma_2|^2}{3\varphi} + \frac{\left(-\frac{|\sigma_2|}{3} - P_l\right)^2}{\psi}}}}$$

Step 3: Identification of φ and A at different temperatures

$$Y = -\frac{(n+1)}{2} ln\left(\left(\frac{\frac{2|\sigma_z|^2}{3} + \frac{|\sigma_z|(\dot{\varepsilon}_z + 2\dot{\varepsilon}_r)\left(-\frac{|\sigma_z|}{3} - P_l\right)}{(\dot{\varepsilon}_r - \dot{\varepsilon}_z)}}{1-\theta}\right)^{\frac{n-1}{n+1}} \left(-\frac{2|\sigma_z|}{3\dot{\varepsilon}_z} + \frac{|\sigma_z|(\dot{\varepsilon}_z + 2\dot{\varepsilon}_r)}{3\dot{\varepsilon}_z(\dot{\varepsilon}_r - \dot{\varepsilon}_z)}\right)^{\frac{2}{n+1}}\right)$$

$$= ln\big(A(T,G)\big) - \mu\left(\frac{(n+1)}{2} ln\left(1 - \frac{\theta}{\theta_c}\right)\right)$$

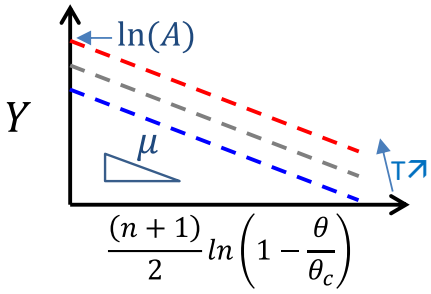

A φ

$$\varphi = \left(1 - \frac{\theta}{\theta_c}\right)^{\mu}$$

$$A(T) = \exp(origin)$$

Step 4: Identification of ψ

$$\frac{\varphi}{\psi} = \frac{|\sigma_z|(\dot{\varepsilon}_z + 2\dot{\varepsilon}_r)}{\left(-\frac{|\sigma_z|}{3} - P_l\right)(\dot{\varepsilon}_r - \dot{\varepsilon}_z)}$$

ψ

Figure 2 The four main steps of this study are presented in this figure : from the experiment and curve calculation, (with the point indication the height and diameter velocity step 1) to the step by step identification of "n" (step 2), A and φ (step 3) and the bulk modulus ψ (step 4); the identification equation are highlighted in blue.

4. Results and discussions

In this section, we provide a detailed explanation of the identification method from steps 1 to 4. Subsequently, the sintering parameters are utilized to simulate sinter-forging tests and achieve complex shape densification through Finite Element Method (FEM) simulation.

4.1. Sinter-forging curves

The sinter-forging curves (step 1) are presented in figure 3. The specimen height curves (figure 3a) exhibit, as expected, an increasing magnitude of shrinkage at higher temperatures. In figure 3b, the diametric evolution is reported. In comparison to the height displacement curves, the diameter evolution curves have significantly lower magnitudes, indicating that the sintering stress due to capillarity forces is of a similar order of magnitude to the applied stress. At 1200°C and 20 MPa, the diameter initially increases, then halts, and slowly decreases in the middle of the dwell. This intriguing behavior emphasizes that the influence of applied stress is more pronounced at the beginning of the dwell, and at a certain point, the impact of capillarity stresses becomes stronger. This highlights the fact that the capillarity stress evolves and increases with the porosity elimination as modeled by Skorohod[40] (3). For 1200°C and 30 MPa, it is interesting to see the specimen diameter slowly decreases despite the higher applied pressure. This indicates the 5-10% higher relative density of the 30 MPa test (see figure 3c), has a greater effect on the capillarity stress because of its porosity dependence (3). Concerning the tests at 1000°C and 1100°C, they are generally recorded in a lower relative density, ranging from 0.55 to 0.7, and the applied stress dominates involving a diameter increase. The diameter evolution curves, in addition to facilitating the identification of sintering parameters, provide a clear indication of the significance of sintering stress under varying conditions. These sintering data serve as the primary input for identification steps 1 to 4.

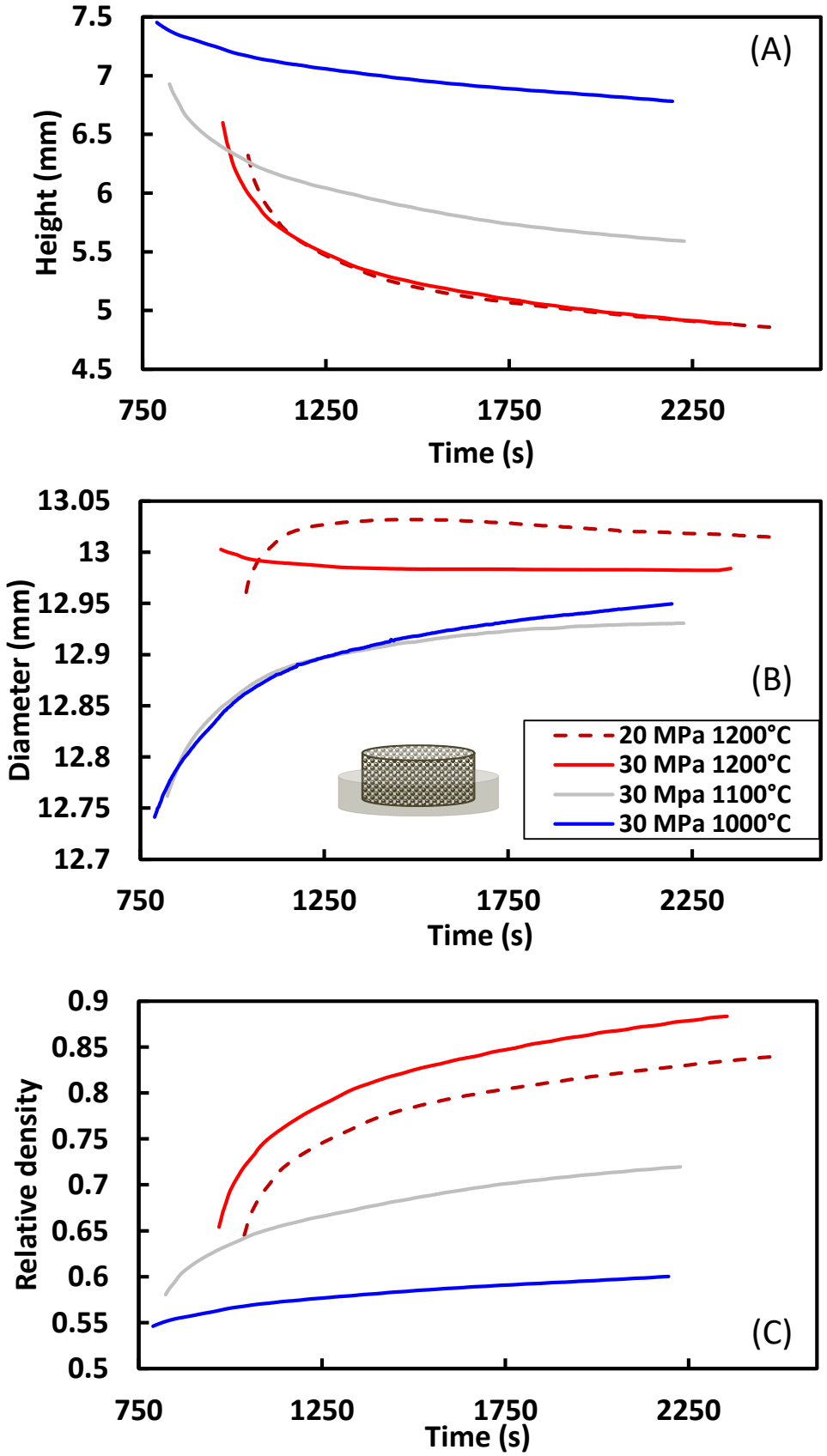

Figure 3 Sinter-forging curves in the isobar, isotherm regime (step 1) with the specimen height (A), diameter (B) and relative density (C).

4.2. Identification of the creep A term and of the shear and bulk moduli

The stress exponent has been determined in [38] (step 2) and is 2.3. The step 3 consists in the assessment of the *A* creep term and the shear modulus using the regression equation (12). This regression is reported in figure 4a for the sinter-forging tests at 1000, 1100 and 1200°C. The slopes of the 1100 and 1200°C tests converge to a same value of μ exponent of 3.9. For 1000°C only, the slope is similar except for the first points corresponding to low relative densities. The model represented by the dotted curve takes a fixed 3.9 value of μ for all the temperatures. The origin gave the A value for each temperature. The temperature dependence of A is then determined by the regression equation (14) and is reported in figure 4b.

$$ln(AT) = ln(A_0) - \frac{Q}{RT} \quad (14)$$

This regression gives the following values for the creep terms: A_0=5.54E-3K.S^{-1}.Pa^{-n} and Q=483kJ.mol^{-1}. This activation energy is close to the literature values of 440kJ.mol^{-1}[28], 430kJ.mol^{-1}[44], 487kJ.mol^{-1}[45] that are attributed to grain boundary diffusion.

Knowing A_0, Q, and φ , the bulk modulus ψ can be determined using equation (9) and the strain rates data (step 4). The obtained shear and bulk moduli are reported in figure 5. All the curves at the different temperatures and pressures converge to similar moduli functions that depend only of the porosity. These moduli porosity functions have been fitted by porosity mathematical function reported on the graph. These functions are very useful to implement the moduli in a finite element software. The unicity of the porosity dependence of these moduli confirms the surface diffusion does not disturb the porosity skeleton. The latter is known to be minimized by the high heating rate (100 K.min^{-1}) [32,33].

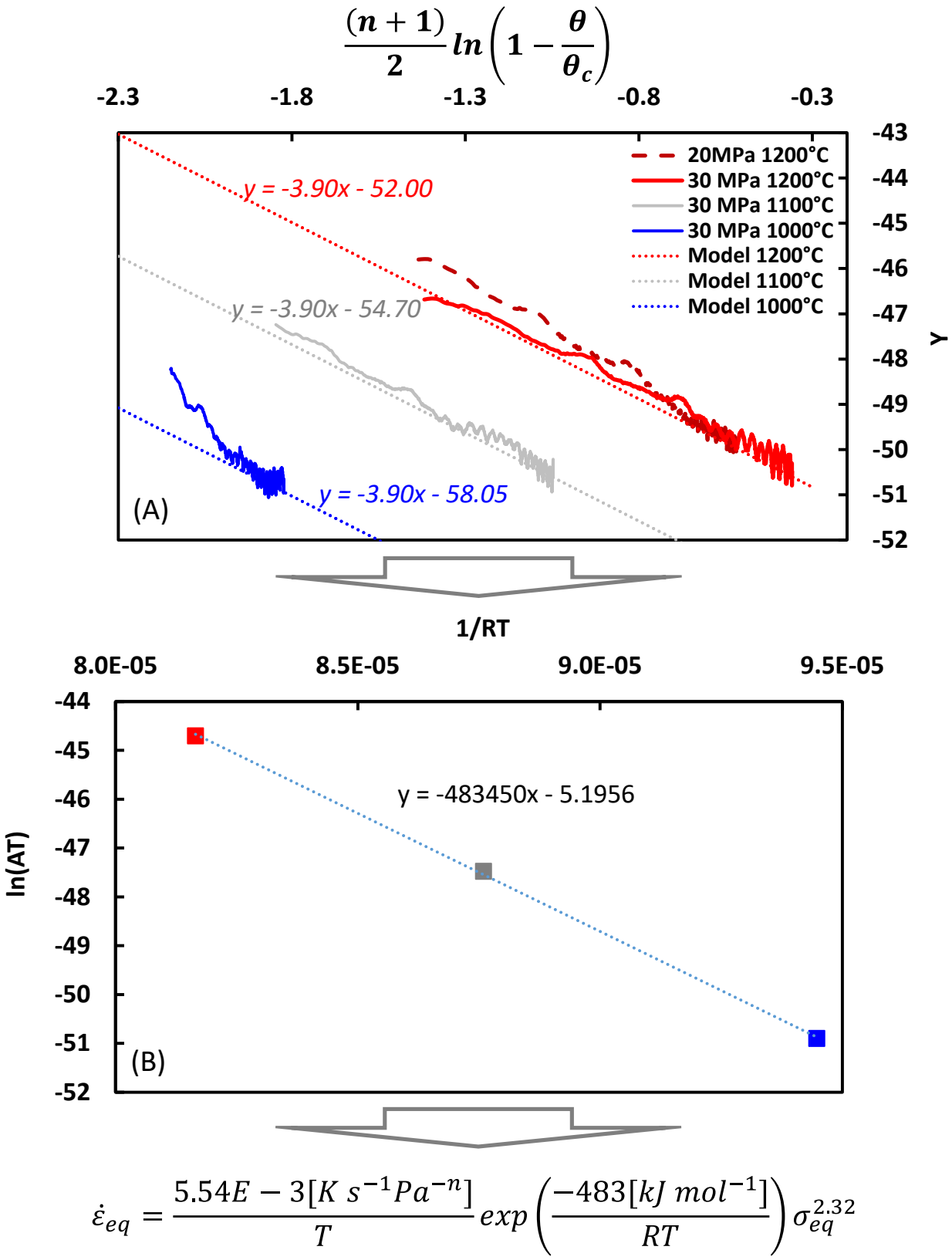

Figure 4 Step 3 of the identification process, (A) graph of the linear regression giving the shear modulus exponent by the slope and A by the origin; (B) determination of the A(T) temperature dependent terms A_0 and Q.

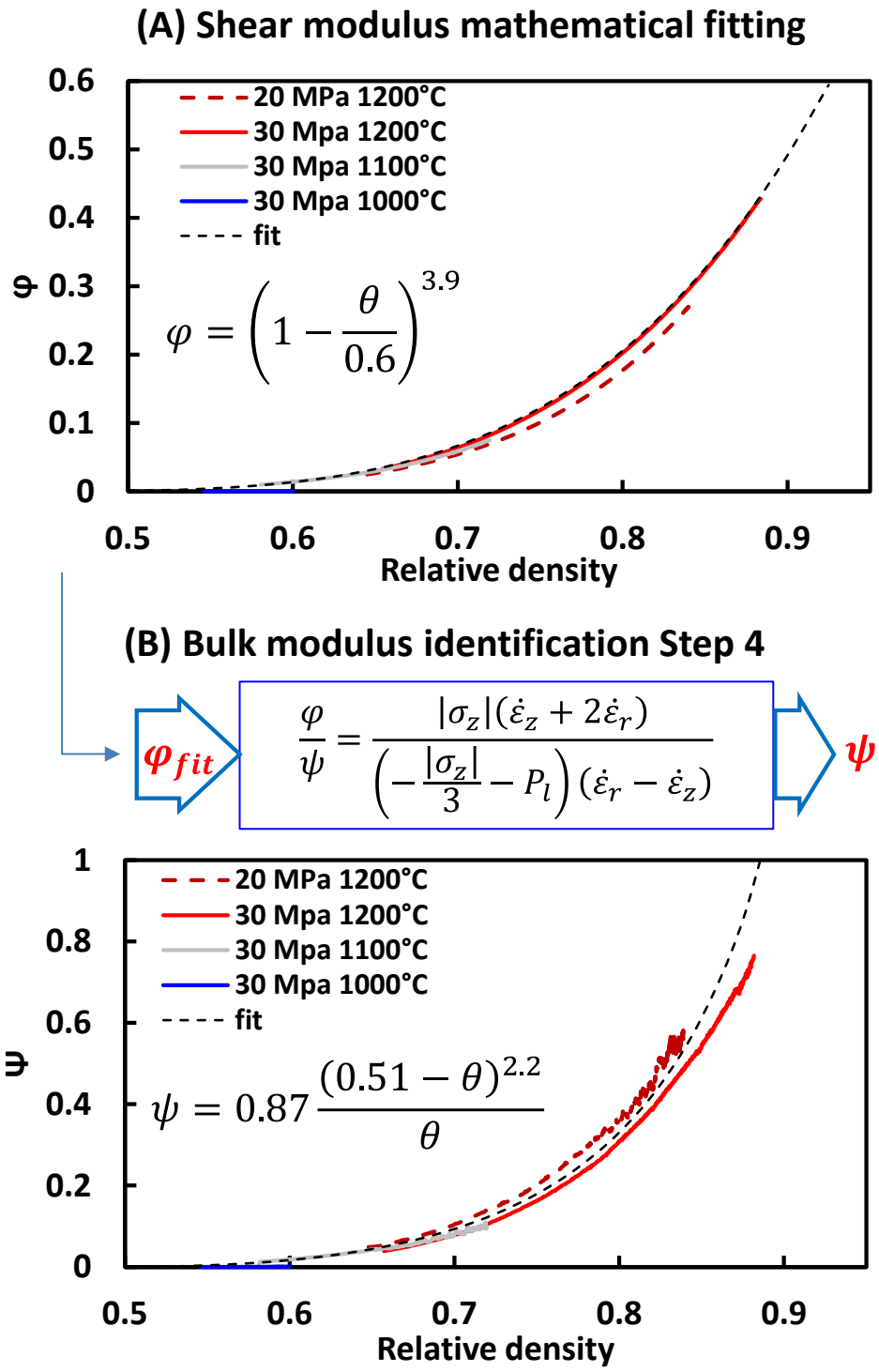

Figure 5 Graph of the obtained experimental moduli and their mathematical fit equation, (A) shear modulus fitting, (B) step 4 of identification of the bulk modulus and fitting.

4.3. Verification of the sintering model by the finite element simulation of the tests

In figure 5, it appears clearly that the experimental moduli data converge to a unique function. However, there is still a small experimental noise and when the mathematical fitting of the data

is conducted, different fitting scenarios are tested and compared to the simulation of the specimens' experimental dimensional curves. The same can be done for the fitting of figure 4a data. In order to conduct this verification, the sinter-forging data have been incorporated in the finite element code using the Skorohod-Olevsky model. The experimental data of the specimen's height, diameter and relative density were compared to the finite element results. These simulations are reported in figure 6 for the best data fitting. This shows that the unique set of sintering parameters reproduces well the axial and radial dimensional changes of the specimen for all the sinter-forging tests with an error of less than 5%. Even the test at 1000°C, where the model fitting in figure 4a was not well adjusted, has a very acceptable reproduction of the sintering curves in figure 6a. Compared to a reduced study limited to a few tests verification, the fact that a unique model reproduces the experimental data in very different experimental conditions is a very positive result. The discrepancy observed can be due to small temperature heterogeneity which can be present for microwave sintering and under high heating rate like 100K/min.

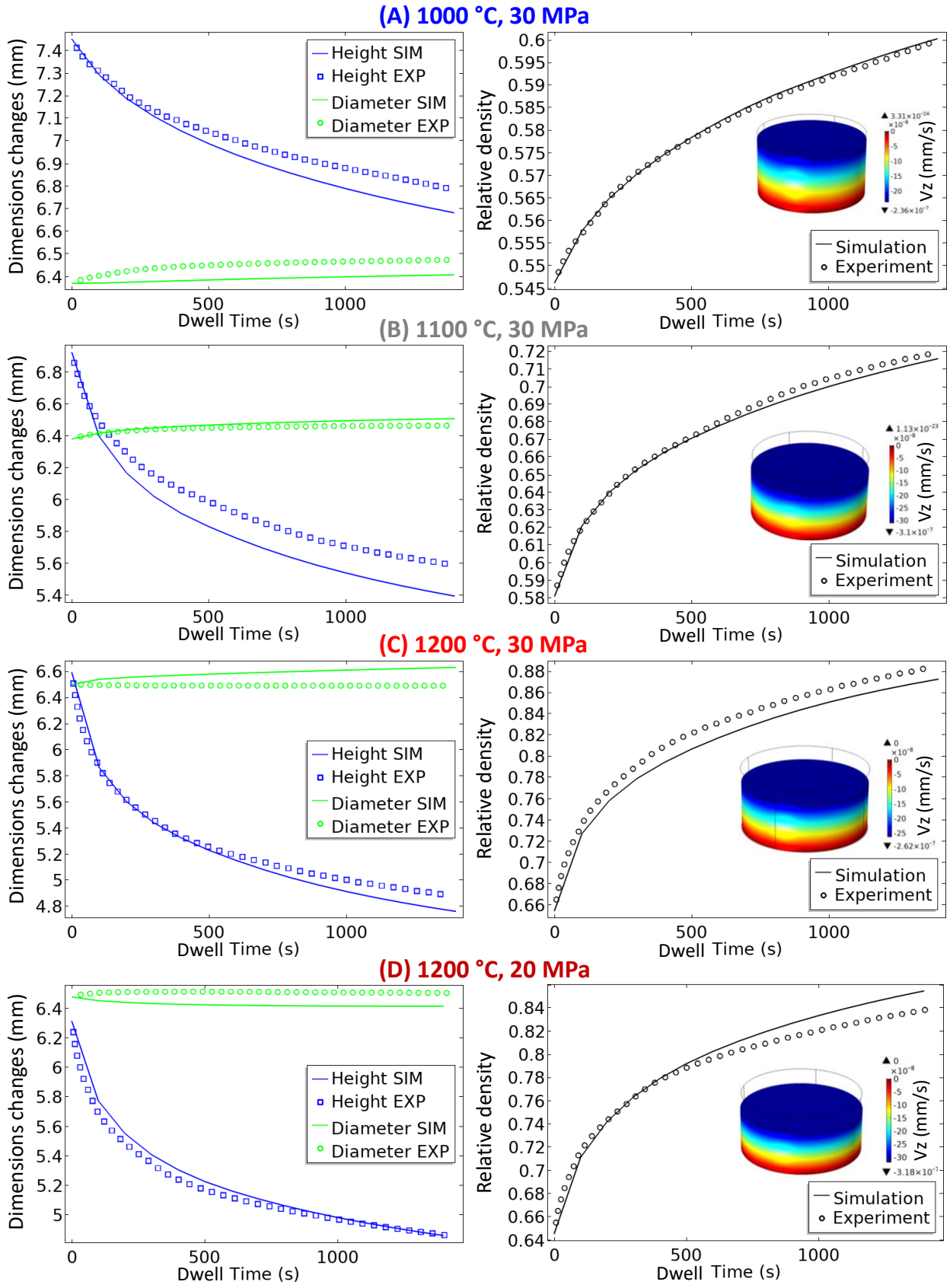

Figure 6 Verification of the finite-element model by the simulation of the sinter-forging tests.

4.4. Comparison of the obtained moduli with the literature theory and to other experimental moduli

Commenting on the experimental moduli is challenging as they reflect the geometry of the porosity skeleton. Nevertheless, it is insightful to compare their values with theoretical and experimental moduli reported in the literature. In figure 7, the obtained moduli are plotted with theoretical moduli assuming spherical porosity (dominant surface diffusion mechanism that reorganizes the pore shape) and other moduli extracted from the literature for ceramics. The theoretical moduli are based on plasticity or creep behavior [16,39]. For Skorohod-Olevsky model, the moduli with the lowest value corresponds to the highest stress intensification and high sintering responsiveness [32]. As expected, the theoretical moduli that assumes spherical porosity are very close and have the highest values and a poor sintering responsiveness. On the contrary, all the experimental moduli of ceramics have clearly lower values than the theoretical one meaning the pore spheroidization by surface diffusion is not dominant in real ceramic microstructures. These are more reactive than the classic theory expected sintering response and could more easily simulate rapid or flash sintering processes if experimentally determined [32]. The moduli obtained in this study have values in the middle range of the other experimental ceramic values.

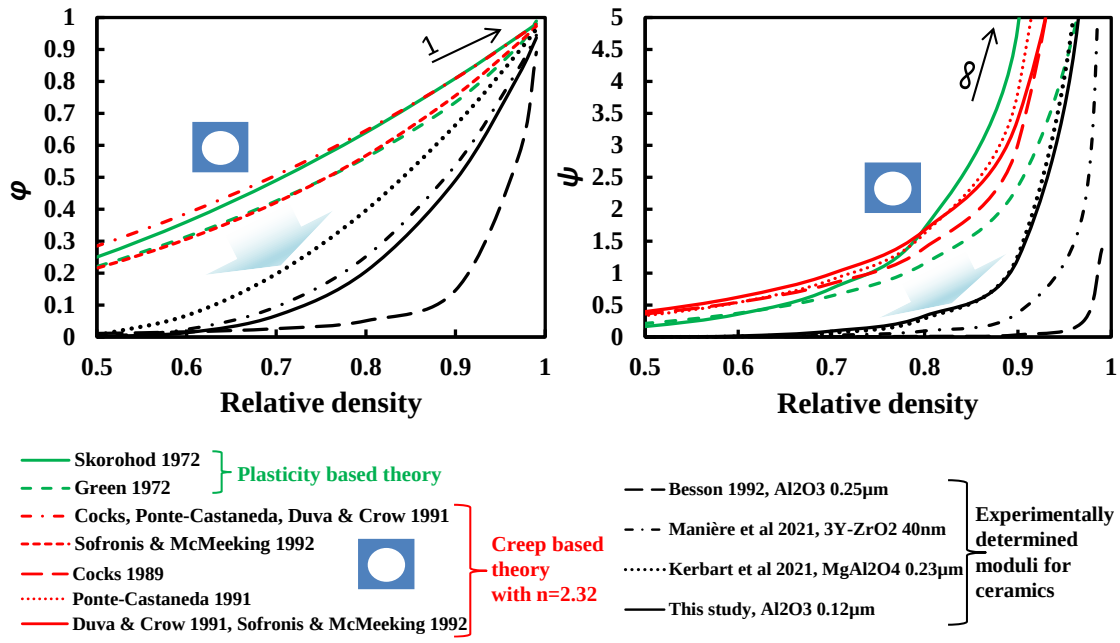

Figure 7 Comparison of the obtained experimental moduli with other experimental and theoretical moduli.

4.5. Test of the model for the finite element simulation of a complex shape hot pressing

Lastly, the finite element model is tested using a complex shape to assess its capability in addressing real pressing issues and detecting the densification gradients induced by the irregularities of complex shapes. In this simulation test, we explore the hot pressing of a complex shape characterized by significant thickness variations. These variations necessitate dissimilar sintering shrinkage and may lead to porosity zones within the part. The simulation conditions and results are presented in figure 8. We simulate the pressing powder zone shape by the following boundary conditions. A fixed displacement is imposed on the lower punches horizontal surfaces, roller condition are imposed on the radial surfaces and we applied 30MPa on the upper horizontal surfaces. A free tetrahedral mesh is used to discretize the powder zone shapes. The temperature is uniform and fixed at 1200°C from the beginning to simulate the case of a heating and a “hot pressing” of the sample. The distribution of the von Mises stress and the relative density is presented in the lower part of figure 8. The areas with higher thicknesses clearly exhibit lower stress and higher porosity. This outcome is expected, given that these zones with greater thicknesses require 1.5 times more shrinkage than the rest of the shape. As

the rest of the shape approaches full densification, the punches stop, and the zones with high thicknesses remain porous. The fact that these zones are more porous results in less stress in these areas. The denser zones bear the primary stress for the entire shape. This simulated tool can be utilized to analyze the densification behavior of ceramic powders under different temperatures, pressures, and shapes. Among the possible applications in pressure assisted sintering simulation, we have: the simulation of densification gradient in hot pressing devices, the study of the deformations induced by container in hot isostatic pressing, the study of porosity originated from temperature gradients in unconventional heating processes like spark plasma sintering, microwave sintering, flash sintering or in forming processes, *etc*.

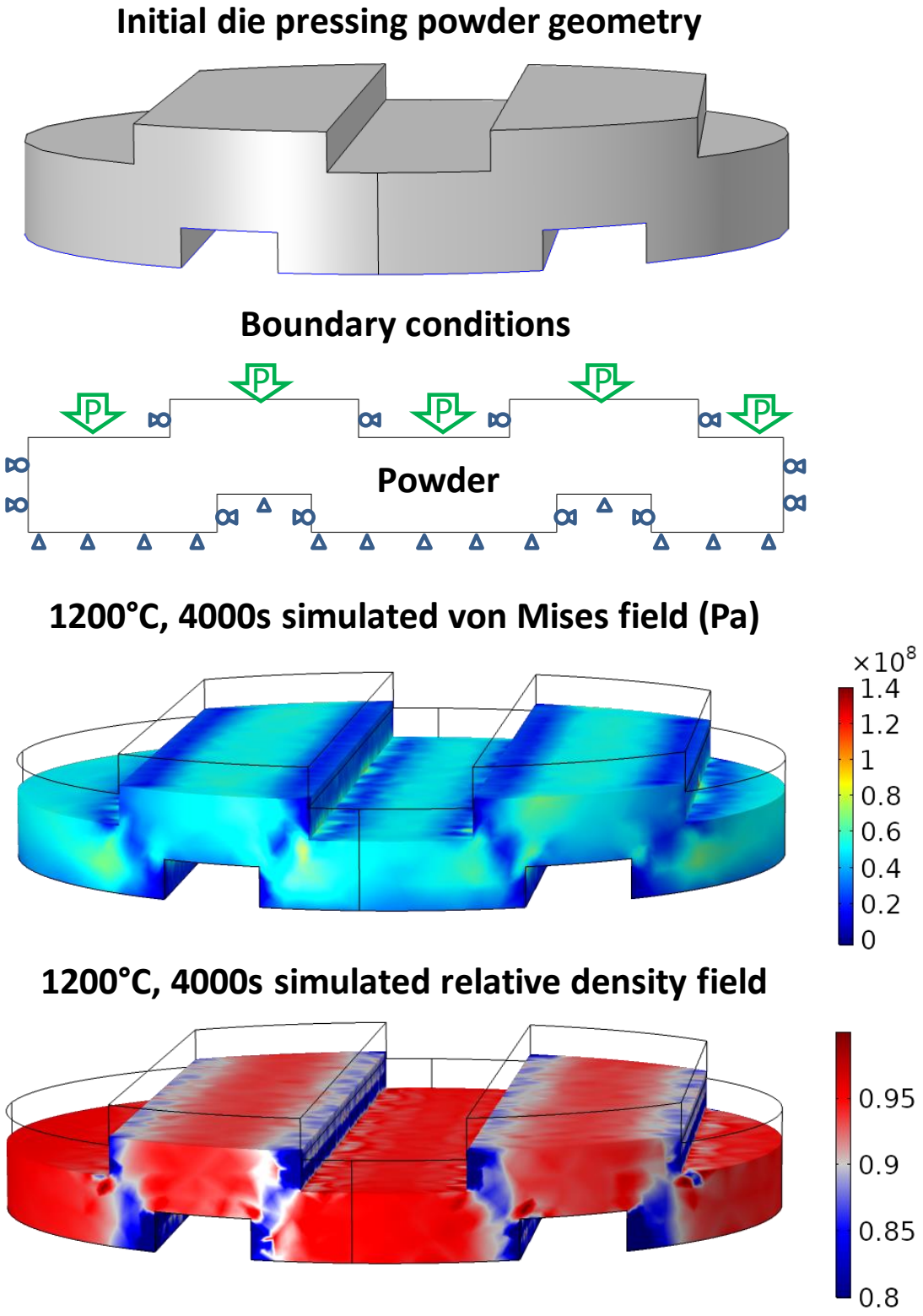

Figure 8 Simulation example of a multi-thicknesses complex shape hot pressing using the identified sintering model.

5. Conclusion

The high interdependence of sintering model parameters to final stage grain growth is a great challenge severely limiting the pressure assisted sintering model assessment method for ceramic powders. In this study, we present a comprehensive method based on sinter-forging tests to solve this problem. Unlike our previous approach, this new method incorporates the sintering stress and is instrumented to significantly limit the extensive iterations tests that involved a high sensitivity to experimental discrepancies. The method is then perfectly suited to assess the sintering behavior of ceramic nanopowders having high sintering stress. It allows fast heating (100 K/min) while the exploration of the moduli and ceramic underlying creep behavior.

This method identified an activation energy of 483 kJ/mol, a value in reasonable agreement with the literature, corresponding to grain boundary diffusion. Concerning the moduli, they converge to a unique porosity function regardless of temperature and pressure conditions. This confirms the sintering theory associating a single porosity function for sintering in close conditions. Given the high dependence of these moduli on porosity geometry, their consistency in experiments with rapid prior heating suggests reduced surface diffusion. The experimental moduli identified falls within a similar range as the few rare other experimental moduli in the literature. This new method can be used to generate more experimental data on sintering moduli, which is still very limited in the literature for ceramics.

Acknowledgements

The help and support of Jérôme Lecourt is gratefully acknowledged. The project Normandy region - 00016601-20E02057_RIN RECHERCHE 2020 - Emergent – ULTIMODULUS support this study.

References

[1] R.K. Bordia, S.-J.L. Kang, E.A. Olevsky, Current understanding and future research directions at the onset of the next century of sintering science and technology, J. Am. Ceram. Soc. 100 (2017) 2314–2352. https://doi.org/10.1111/jace.14919.

[2] S. Grasso, Y. Sakka, G. Maizza, Electric current activated/assisted sintering (ECAS): a review of patents 1906–2008, Sci. Technol. Adv. Mater. 10 (2009) 053001.

https://doi.org/10.1088/1468-6996/10/5/053001.
[3] O. Guillon, J. Gonzalez-Julian, B. Dargatz, T. Kessel, G. Schierning, J. Räthel, M. Herrmann, Field-Assisted Sintering Technology/Spark Plasma Sintering: Mechanisms, Materials, and Technology Developments, Adv. Eng. Mater. 16 (2014) 830–849. https://doi.org/10.1002/adem.201300409.
[4] R. Orrù, R. Licheri, A.M. Locci, A. Cincotti, G. Cao, Consolidation/synthesis of materials by electric current activated/assisted sintering, Mater. Sci. Eng. R Reports. 63 (2009) 127–287. https://doi.org/10.1016/j.mser.2008.09.003.
[5] R.M. German, Sintering With External Pressure, in: Sinter. from Empir. Obs. to Sci. Princ., Elsevier, 2014: pp. 305–354. https://doi.org/10.1016/B978-0-12-401682-8.00010-0.
[6] M.N. Rahaman, Sintering of Ceramics, CRC Press, 2007.
[7] B.R. Golla, A. Mukhopadhyay, B. Basu, S.K. Thimmappa, Review on ultra-high temperature boride ceramics, Prog. Mater. Sci. 111 (2020) 100651. https://doi.org/10.1016/j.pmatsci.2020.100651.
[8] Z. Xiao, S. Yu, Y. Li, S. Ruan, L.B. Kong, Q. Huang, Z. Huang, K. Zhou, H. Su, Z. Yao, W. Que, Y. Liu, T. Zhang, J. Wang, P. Liu, D. Shen, M. Allix, J. Zhang, D. Tang, Materials development and potential applications of transparent ceramics: A review, Mater. Sci. Eng. R Reports. 139 (2020) 100518. https://doi.org/10.1016/j.mser.2019.100518.
[9] A. Goldstein, A. Krell, Transparent Ceramics at 50: Progress Made and Further Prospects, J. Am. Ceram. Soc. 99 (2016) 3173–3197. https://doi.org/10.1111/jace.14553.
[10] R. Orrù, G. Cao, Ultra-high temperature ceramics by spark plasma sintering, in: Spark Plasma Sinter., Elsevier, 2019: pp. 49–76. https://doi.org/10.1016/B978-0-12-817744-0.00002-7.
[11] E.A. Olevsky, D. V. Dudina, Field-Assisted Sintering, Springer N, Springer International Publishing, Cham, 2018. https://doi.org/10.1007/978-3-319-76032-2.
[12] R.M. German, Sintering Theory and Practice, Wiley, Wiley, 1996. http://www.wiley.com/WileyCDA/WileyTitle/productCd-047105786X.html.
[13] H.J. Frost, M.F. Ashby, Deformation-Mechanism Maps, The Plasticity and Creep of Metals and Ceramics, Pergamon P, Oxford, 1982. http://engineering.dartmouth.edu/defmech/.
[14] A.S. Helle, K.E. Easterling, M.F. Ashby, Hot-isostatic pressing diagrams: New developments, Acta Metall. 33 (1985) 2163–2174. https://doi.org/10.1016/0001-6160(85)90177-4.
[15] E. Arzt, M.F. Ashby, K.E. Easterling, Practical applications of hotisostatic Pressing diagrams: Four case studies, Metall. Trans. A. 14 (1983) 211–221. https://doi.org/10.1007/BF02651618.
[16] C. Manière, C. Harnois, S. Marinel, Porous stage assessment of pressure assisted sintering modeling parameters: a ceramic identification method insensitive to final stage grain growth disturbance, Acta Mater. 211 (2021) 116899. https://doi.org/10.1016/j.actamat.2021.116899.
[17] M. Abouaf, J.L. Chenot, A numerical model for hot deformation of metal powders, J. Theor. Appl. Mech. 5 (1986) 121–140.
[18] M. Abouaf, PhD, Modélisation de la compaction de poudres métalliques frittées, approches par la mécanique des milieux continus, Institut national polytechnique de Grenoble, 1985.
[19] C. Nicolle, PhD, Mise en forme de poudre de bore par compression isostatique à chaud: determination des propriétés rhéologiques et simulation numérique du procédé, Université de Bourgogne, France, 1999.
[20] C. Geindreau, D. Bouvard, P. Doremus, Constitutive behaviour of metal powder during hot forming. Part I: Experimental investigation with lead powder as a simulation material, Eur. J. Mech. - A/Solids. 18 (1999) 581–596. https://doi.org/10.1016/S0997-

7538(99)00102-3.
[21] C. Geindreau, D. Bouvard, P. Doremus, Constitutive behaviour of metal powder during hot forming.: Part II: Unified viscoplastic modelling, Eur. J. Mech. - A/Solids. 18 (1999) 597–615. https://doi.org/10.1016/S0997-7538(99)00101-1.
[22] Y. Xue, L.H. Lang, G.L. Bu, L. Li, Densification modeling of titanium alloy powder during hot isostatic pressing, Sci. Sinter. 43 (2011) 247–260. https://doi.org/10.2298/SOS1103247X.
[23] C. Wolff, S. Mercier, H. Couque, A. Molinari, Modeling of conventional hot compaction and Spark Plasma Sintering based on modified micromechanical models of porous materials, Mech. Mater. 49 (2012) 72–91. https://doi.org/10.1016/j.mechmat.2011.12.002.
[24] D. Martins, F. Grumbach, C. Manière, P. Sallot, K. Mocellin, M. Bellet, C. Estournès, In-situ creep law determination for modeling Spark Plasma Sintering of TiAl 48-2-2 powder, Intermetallics. 86 (2017) 147–155. https://doi.org/10.1016/j.intermet.2017.03.006.
[25] C. Manière, E.A. Olevsky, Porosity dependence of powder compaction constitutive parameters: Determination based on spark plasma sintering tests, Scr. Mater. 141 (2017) 62–66. https://doi.org/10.1016/j.scriptamat.2017.07.026.
[26] C. Manière, J.S. Diatta, C. Couder, C. Harnois, S. Marinel, Spark plasma sintering grain growth assessment by densification kinetics analysis, Scr. Mater. 228 (2023) 115346. https://doi.org/10.1016/j.scriptamat.2023.115346.
[27] J.S. Diatta, C. Couder, C. Harnois, S. Marinel, C. Manière, Modeling spark plasma sintering of zirconia with prediction of final stage high densification rate, Mater. Lett. 337 (2023) 133930. https://doi.org/10.1016/j.matlet.2023.133930.
[28] J. Wang, R. Raj, Estimate of the Activation Energies for Boundary Diffusion from Rate-Controlled Sintering of Pure Alumina, and Alumina Doped with Zirconia or Titania, J. Am. Ceram. Soc. 73 (1990) 1172–1175. https://doi.org/10.1111/j.1151-2916.1990.tb05175.x.
[29] H. Su, D.L. Johnson, Master Sintering Curve: A Practical Approach to Sintering, J. Am. Ceram. Soc. 79 (1996) 3211–3217. https://doi.org/10.1111/j.1151-2916.1996.tb08097.x.
[30] O. Guillon, J. Langer, Master sintering curve applied to the Field-Assisted Sintering Technique, J. Mater. Sci. 45 (2010) 5191–5195. https://doi.org/10.1007/s10853-010-4556-7.
[31] C. Manière, L. Durand, G. Chevallier, C. Estournès, A spark plasma sintering densification modeling approach: from polymer, metals to ceramics, J. Mater. Sci. 53 (2018) 7869–7876. https://doi.org/10.1007/s10853-018-2096-8.
[32] C. Manière, C. Harnois, S. Marinel, Role of microstructure reactivity and surface diffusion in explaining flash (ultra-rapid) sintering kinetics, J. Eur. Ceram. Soc. 43 (2023) 2057–2068. https://doi.org/10.1016/j.jeurceramsoc.2022.12.006.
[33] E.A. Olevsky, S. Kandukuri, L. Froyen, Consolidation enhancement in spark-plasma sintering: Impact of high heating rates, J. Appl. Phys. 102 (2007) 114913. https://doi.org/10.1063/1.2822189.
[34] W. Ji, J. Zhang, W. Wang, Z. Fu, R.I. Todd, The microstructural origin of rapid densification in 3YSZ during ultra-fast firing with or without an electric field, J. Eur. Ceram. Soc. 40 (2020) 5829–5836. https://doi.org/10.1016/j.jeurceramsoc.2020.07.027.
[35] R.I. Todd, E. Zapata-Solvas, R.S. Bonilla, T. Sneddon, P.R. Wilshaw, Electrical characteristics of flash sintering: thermal runaway of Joule heating, J. Eur. Ceram. Soc. 35 (2015) 1865–1877. https://doi.org/10.1016/j.jeurceramsoc.2014.12.022.
[36] M.-Y. Chu, M.N. Rahaman, L.C. Jonghe, R.J. Brook, Effect of Heating Rate on Sintering and Coarsening, J. Am. Ceram. Soc. 74 (1991) 1217–1225. https://doi.org/10.1111/j.1151-2916.1991.tb04090.x.
[37] C. Manière, C. Harnois, G. Riquet, T. Grippi, S. Behar-Lafenetre, S. Marinel, Rapid microwave sintering of centimetric zirconia: Scalability and electromagnetic-thermal-

fluid-dynamic simulation, J. Am. Ceram. Soc. (2022). https://doi.org/10.1111/jace.18787.
[38] C. Manière, J.S. Diatta, C. Harnois, C. Couder, C. Bilot, S. Marinel, Pressure assisted sintering stress exponent assessment methods: Accuracy analysis and effect of sintering stress, Mech. Mater. 181 (2023) 104664. https://doi.org/10.1016/j.mechmat.2023.104664.
[39] E.A. Olevsky, Theory of sintering: from discrete to continuum, Mater. Sci. Eng. R Reports. 23 (1998) 41–100. https://doi.org/10.1016/S0927-796X(98)00009-6.
[40] V.V. Skorohod, Rheological basis of the theory of sintering, Nauk. Dumka, Kiev. (1972).
[41] E.A. Olevsky, C. Garcia-Cardona, W.L. Bradbury, C.D. Haines, D.G. Martin, D. Kapoor, Fundamental Aspects of Spark Plasma Sintering: II. Finite Element Analysis of Scalability, J. Am. Ceram. Soc. 95 (2012) 2414–2422. https://doi.org/10.1111/j.1551-2916.2012.05096.x.
[42] W. Li, E.A. Olevsky, J. McKittrick, A.L. Maximenko, R.M. German, Densification mechanisms of spark plasma sintering: multi-step pressure dilatometry, J. Mater. Sci. 47 (2012) 7036–7046. https://doi.org/10.1007/s10853-012-6515-y.
[43] C. Manière, T. Grippi, S. Marinel, Estimate microstructure development from sintering shrinkage: A kinetic field approach, Mater. Today Commun. 31 (2022) 103269. https://doi.org/10.1016/j.mtcomm.2022.103269.
[44] J. Langer, M.J. Hoffmann, O. Guillon, Direct comparison between hot pressing and electric field-assisted sintering of submicron alumina, Acta Mater. 57 (2009) 5454–5465. https://doi.org/10.1016/j.actamat.2009.07.043.
[45] G. Antou, P. Guyot, N. Pradeilles, M. Vandenhende, A. Maître, Identification of densification mechanisms of pressure-assisted sintering: application to hot pressing and spark plasma sintering of alumina, J. Mater. Sci. 50 (2015) 2327–2336. https://doi.org/10.1007/s10853-014-8804-0.